



Effect of Rotational Speed on Microstructure and Mechanical Properties of 2060 Aluminum Alloy RFSSW Joint

Peng Chai^{1,2} · Yue Wang^{1,2}

Received: 8 February 2019 / Accepted: 6 May 2019 / Published online: 16 May 2019
© The Korean Institute of Metals and Materials 2019

Abstract

Refill friction stir spot welding (RFSSW) is used to weld 3.2-mm-thick 2060 aluminum alloy sheets. In this study, we investigated the formation, microstructures and mechanical properties of the RFSSW joint. The results show that increasing the rotational speed is beneficial to eliminating annular groove but increasing the flash. The hook of the joint at each rotational speed is downward bending. The void at the bottom of the sleeve-affected zone (SAZ) and incomplete bonding at the lap interface initially increase and then decrease with the rotational speed increments from 2000 to 2600 rpm. The microstructure distribution at the bottom of the stir zone (SZ) is similar to that at the interface of the SAZ/thermo-mechanically affected zone (TMAZ), including SZ, TMAZ, heat-affected zone, and the base material. The microhardness values of the joint gradually decrease along the sheet thickness at each welding condition. Furthermore, the microhardness at the SAZ/TMAZ interface initially increases to the maximum at 2400 rpm and then decrease to the minimum at 2600 rpm. Moreover, the tensile-shear failure load of the joint initially increases and then decreases with increasing rotational speeds. The fracture positions of tensile-shear specimens are related to microstructure distribution, microhardness, material flow, and welding defects.

Keywords Refill friction stir spot welding · 2060 Aluminum alloy · Microstructure · Mechanical properties

1 Introduction

Owing to the requirement of lightweight materials in manufacturing industries, many series of aluminum alloys are extensively used in aviation, aerospace, automotive, and shipbuilding [1–3]. A high composition of Li in aluminum alloys decreases the weight and improves the mechanical properties of these materials [4]. Recently, third-generation aluminum–lithium alloys have been identified as excellent candidates for developing aircrafts components [5–7], in which saving weight is very crucial. Therefore, aluminum–lithium alloys can be important materials for manufacturing industries. Note that in aviation structures lap joints are extensively used. Drilling prior to connection and weight increment of rivets cannot be avoided when riveting is employed. Unlike line welding, spot joints could reduce

the welding area and then minimize the global deformations of welding structures. However, fusion welding technologies suffer from various disadvantages such as porosity, large heat deformation, and coarse microstructure [8]. Hence, to join these aluminum alloys, a new spot welding method is required.

Friction stir spot welding (FSSW) developed by Mazda Motor Corporation, is a variant of friction stir welding (FSW), and is also considered to be a solid-state welding technology [9]. Unlike FSW, no movement of linear welding is observed during the FSSW process, and this welding process can be divided into three stages. First, the welding tool is rotated at a preset rotational speed. Second, the rotational tool plunges into the welding plates based on the set depth and is remained for some time. Finally, the rotational tool retreats from the welding plates and stops rotating. Hence, FSSW joints possess a keyhole after the tool is retracted from the welding plate. Several new welding methods have been proposed to eliminate this keyhole. Prangnell et al. [10] performed pinless FSSW to weld 6111-T4 aluminum alloy sheets having thickness of 0.91 mm with a high-quality without keyhole being obtained. Sun et al. [11] developed a novel two-step spot FSW of 6061 Al and

✉ Yue Wang
endlesswy@163.com

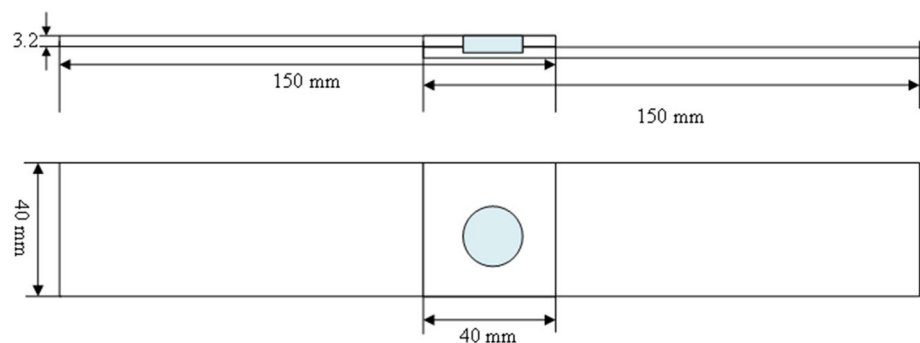
¹ School of Mechanical Engineering and Automation, Beihang University, Beijing 100191, People's Republic of China

² Laboratory of FSW, AVIC Manufacturing Technology Institute, Beijing 100024, People's Republic of China

5052 Al. The results revealed that the obtained surface of joint was smooth, and the joint strength increased compared to materials of 6061 Al and 5052 Al. Han et al. [12] reported that the joint strength improved when using 7075 aluminum alloys bit refilled keyhole in the 2219 alloy FSW joint. Ji et al. [13] filled the keyhole of the AZ31 magnesium alloy FSW joint using the active–passive filling method. Note that the strength of the filled joint reached 96.3% of that of the FSW joint.

Refill FSSW (RFSSW) technology, developed by GKSS in 2002, was evolved from FSSW. Note that its rotational tool has three components, namely, a pin, a sleeve and a clamping ring [14]. During the welding process, the extrusive material was squeezed back into the welding spot using a complex movement of these three components. Therefore, the welding joint without a keyhole was obtained after welding by avoiding the stress concentration caused by an external load [15]. To date, RFSSW has been one of the most promising welding technologies to replace riveting and traditional fusion welding methods. Compared with the above-mentioned filling technologies [10–13], RFSSW simplifies the experimental process. Plaine et al. [16] investigated the effect of process parameters on the mechanical properties of dissimilar alloy joint. The results show that the rotational speed was the predominant factor for controlling the joint tensile-shear strength. With increasing rotational speed, the grains of the heat-affected zone (HAZ) and stir zone (SZ) gradually coarsened for the 6061-T6 aluminum alloy RFSSW joint [17]. Shi et al. [18] reported that the shear failure load of a 2-mm-thick 2198 aluminum alloy joint initially increased and then decreased when the rotational speed increased from 1200 rpm to 1800 rpm. Owing to the low density, high strength, and excellent elastic modulus of aluminum–lithium alloys, their RFSSW has attracted considerable attention. Moreover, the 2060 aluminum–lithium alloy has been extensively used in aerospace [6, 19, 20]. However, there have been very few studies on the RFSSW process of this excellent material. Hence, in this study, we primarily focused on the effect of the rotational speed on the microstructure and mechanical properties of the RFSSW joint.

Fig. 1 Schematic of the tensile-shear specimens



2 Experiment

2060 aluminum–lithium alloy plates with 3.2 mm thickness were selected as the base material (BM), which possesses the following chemical compositions (all in wt%): 3.40 Cu, 0.80 Li, 0.27 Mg, 0.18 Ag, 0.10 Zr, balanced with Al. All the plates with the dimensions of 40 mm × 150 mm were cut perpendicular to the rolling direction. Prior to welding, all the surfaces of lap plates were polished with abrasive papers to eliminate the oxide layer. The overlap area was 40 mm × 40 mm, and the welding spot was located at the center of the overlap area. Figure 1 depicts the schematic of the welding lap joint. The welding machine used in this study was manufactured by Beijing FSW Technology Co., Ltd. Figure 2 shows the welding tool components. The outer diameters of the pin, sleeve and clamping ring are 6, 9 and 18 mm, respectively. After the components were assembled to the welding machine, radial run-out needed to be measured, and the tolerance should be in the range of ± 0.05 mm. During the welding process, the plunge depth was fixed as 4 mm, and plunge speed and refilling speed were both 50 mm/min. The variable was rotational speed, and it was in the range of 2000–2600 rpm.



Fig. 2 Welding tool of the RFSSW

To obtain the cross section, the RFSSW joint was cut along the center of the welding spot. The metallographic samples were burnished using various types of sand papers from #240 to #2000 and then etched using Keller's reagent. The cross-sections and microstructures were observed using an optical microscope (OM) and a scanning electron microscope (SEM), respectively. The microhardness testing points with 0.5 mm testing steps were located at the sleeve-affected zone (SAZ) and the interface between the SAZ and thermo-mechanically affected zone (TMAZ). Moreover, the Wilson hardness tester was used as the testing machine. The tensile-shear test was performed three times for each rotational speed in accordance with the standard of ISO 6892-1-2009 "Metallic materials-Tensile testing-Part 1: Method of test at room temperature". Furthermore, the fracture locations and surfaces were observed using OM and SEM, respectively.

3 Results and Discussion

3.1 Analysis of Formations

Figure 3 shows the surface appearance of the RFSSW joints at different rotational speeds. Unlike FSSW joint, no keyhole was observed in the RFSSW joint, and surface indentation on the welding spots was only minimal. The top surface of the joint was smooth, and no defect on the material adhesion was observed, as reported by Zhao et al. [14]. The annular groove defect partially appeared at the rotational speed of 2000 rpm and then disappeared as the rotational speed

increased. Zhao et al. [14] stated that the annular groove formation was attributed to material loss. Shen et al. [21] and Rosendo et al. [22] reported that poor fluidity of the material was responsible for the annular groove. Note that the annular groove is also related to the flow stress of plastic materials. Generally, the material flow stress reduces with the increasing temperature of the material. Some plastic materials squeezed into the gap between the sleeve and clamping ring during the sleeve plunge process at a low rotational speed cannot completely refill the keyhole because of the high flow stress of the materials. Thus, the annular groove was observed at 2000 rpm. With increasing rotational speed, remarkably soft plastic material was refilled back to the keyhole. Hence, the annular groove disappeared and even the driven material was squeezed out of the keyhole forming the flash, as shown in Fig. 3b–d.

Figure 4 shows the cross-sections of the RFSSW joints at various rotational speeds. The cross section shows a typical U-shape, which is associated with the rotational tool geometry and a characteristic of heat generation. Based on various characteristics of different zones, the RFSSW joint can be clarified into four regions, i.e., BM, SZ, TMAZ and HAZ. SZ was divided into two zones, i.e., SAZ and pin-affected zone (PAZ) with regard to the differences in stirring components. Note that the geometry of the cross-section is symmetrical compared to the axial center of the rotational pin.

Fig. 3 Surface appearance of the RFSSW joints at various rotational speeds: **a** 2000, **b** 2200, **c** 2400 and **d** 2600 rpm

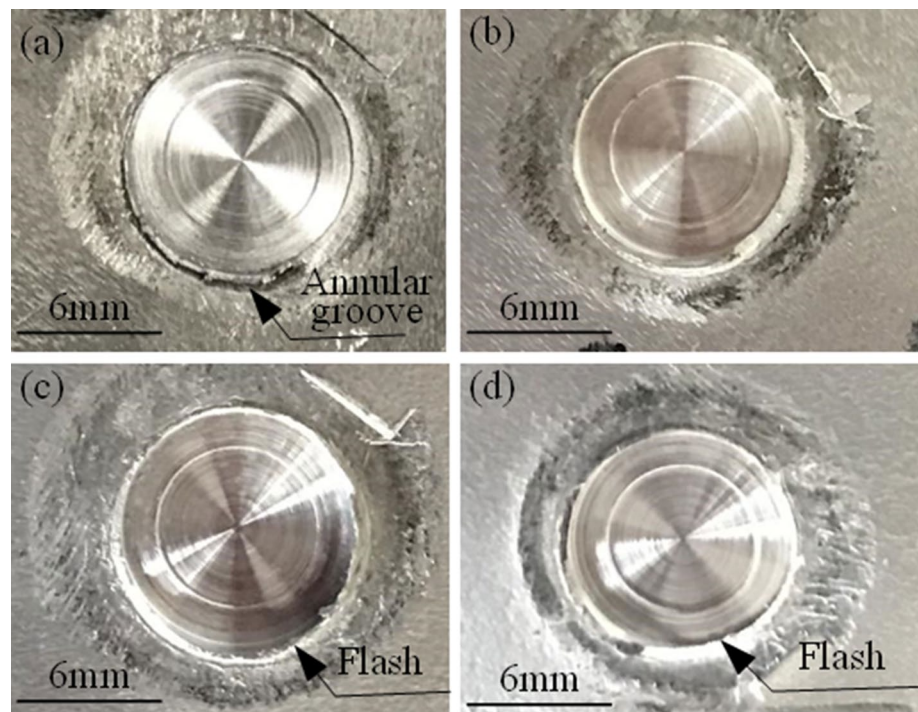
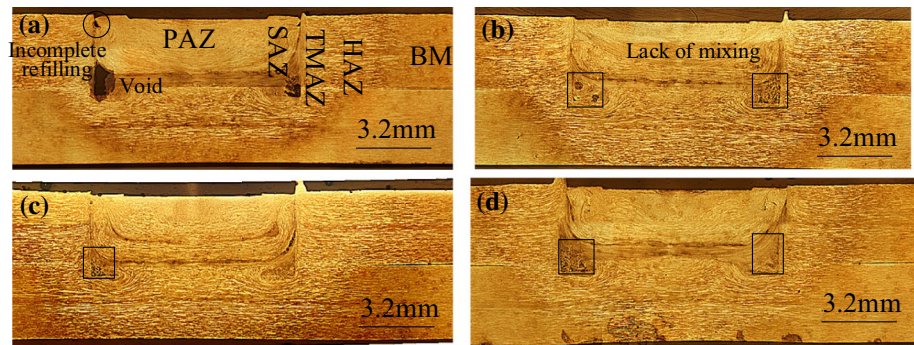


Fig. 4 Cross-sections of the RFSSW joints at various rotational speeds: **a** 2000, **b** 2200, **c** 2400 and **d** 2600 rpm



3.2 Analysis of Defects

As shown in Fig. 4, a void was observed at the bottom of the SAZ. The size and morphology of the void were variable, which could be related to various material flow characteristics of the SZ and material volume filling keyhole. When the rotational speed was the lowest (2000 rpm), the void was the largest and exhibited a rectangular shape. The void became smaller at high rotational speeds and demonstrated the lack of mixing, as shown in Fig. 4b–d. The higher rotational speed generates larger heat input, resulting in minimal flow stress of the plastic material. Accordingly, the material fluidity around the SAZ improved, and more material could be squeezed into the rotational sleeve to refill the keyhole at a high rotational speed. Note that the void became large again when the rotational speed further increased to 2600 rpm. At this rotational speed, large volume of heat softened the material near the rotational sleeve, and then the viscosity coefficient of the material further reduced. On the one hand, the over-softened material cannot be completely refilled back to the keyhole. On the other hand, the physical properties of the material on both sides of the rotational sleeve varied significantly at the refilling stage. Hence, the void at the bottom of the SAZ is caused by complex reasons. However, the formation mechanism of the void cannot be explained by a single reason. The large void at 2000 rpm was primarily attributed to loss of material, and the material used to fill the keyhole formed the flash on the welding spot accompanied with incomplete refilling, as shown in Fig. 4a. The different physical properties of the material on both sides of the sleeve are primarily responsible for the lack of mixing in Fig. 4b–d. The void would reduce the integrity of the welding structure and generate stress concentration under an external load.

As mentioned previously, incomplete refilling is caused by the material loss of the joint and is located at the top surface of the upper sheet, as shown in Fig. 4a. This incomplete refilling corresponds to the annular groove and disappears at high rotational speeds. The welding quality of the welding spot periphery, such as SAZ/TMAZ and lap interfaces, is significant to the mechanical properties of the RFSSW joint [23]. Figure 5 shows the enlarged views of the

SAZ/TMAZ interfaces. The lack of mixing was observed at 2000 rpm and reduced at 2200 rpm, and even disappeared at 2400 and 2600 rpm. During the RFSSW process, the SAZ/TMAZ interface was parallel to the moving direction of the rotational tool, and then it was bonded via atomic diffusion. The temperature was the dominant factor for determining the bonding quality. Moreover, the heat input gradually increased as the rotational speed enhances, leading to increased atomic diffusion rate. Therefore, the lack of mixing partially decreased (Fig. 5b) and then disappeared (Fig. 5c, d).

Owing to the inherent characteristics of RFSSW, the hook is unavoidable when the tool plunges into the lower sheet [21], and it plays an important role on the failure load of the lap joint. Both Parra et al. [24] and Shen et al. [16] obtained a hook with an upside down V shape in 6 series of aluminum alloys RFSSW joint. The upward bending of the hook reduced the effective thickness of the upper sheet, which is detrimental to the tensile load of the RFSSW joint [14]. Moreover, the upward bending hook was reported to be caused by the lower sheet deformation [24]. However, the upward bending hook was not noticeable in the 7075 aluminum alloy RFSSW joint. Shen et al. [16] revealed that the difference in hook geometry was due to the varying plasticity of the material. Li et al. [25] obtained flat, upward, and downward bending hooks in the 2024-T4 aluminum alloy RFSSW joint at various plunge depths. They demonstrated that the hook was related to the plunge depth of the sleeve. However, hook formation is a complex process. Hence, the formation mechanism is difficult to explain by using only a certain factor, such as sleeve depth or plasticity of the material. In this study, the hook was downward bending at each rotational speed, as shown in Fig. 6. Based on the hook geometry, the downward hook was caused by the deformation of the upper sheet. When compared with the previously mentioned 6 series of aluminum alloys, the 2060 aluminum alloy has a higher plastic temperature. Furthermore, the void in the hook's vicinity cannot generate any pressure on the lower sheet. Therefore, the upper sheet was driven by the downward movement of the sleeve to bend downward. With the same plunge depth, the rotational speed had almost no

Fig. 5 SAZ/TMAZ interface at different rotational speeds: **a** 2000, **b** 2200, **c** 2400 and **d** 2600 rpm

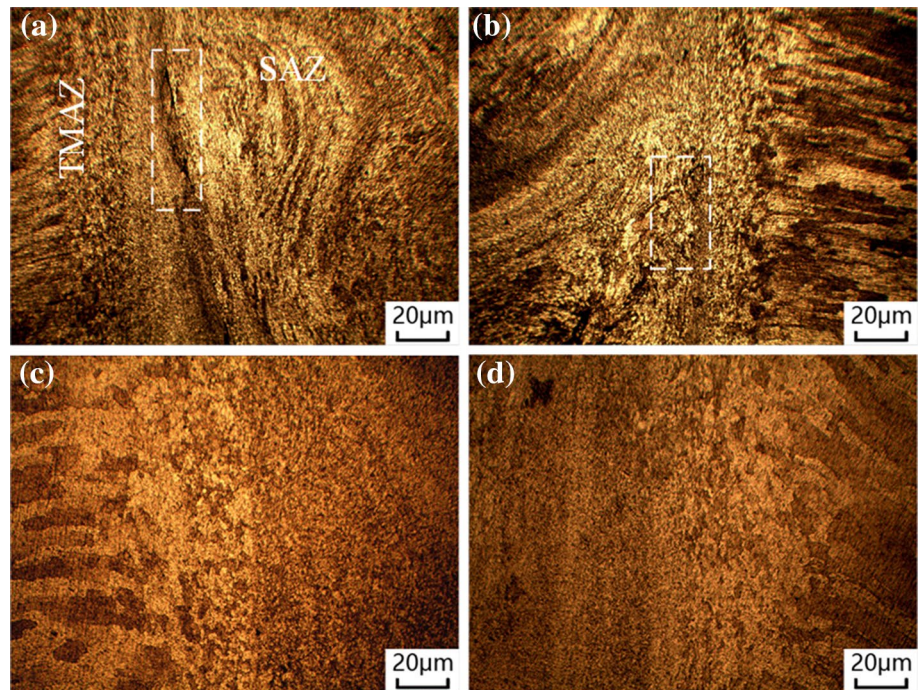
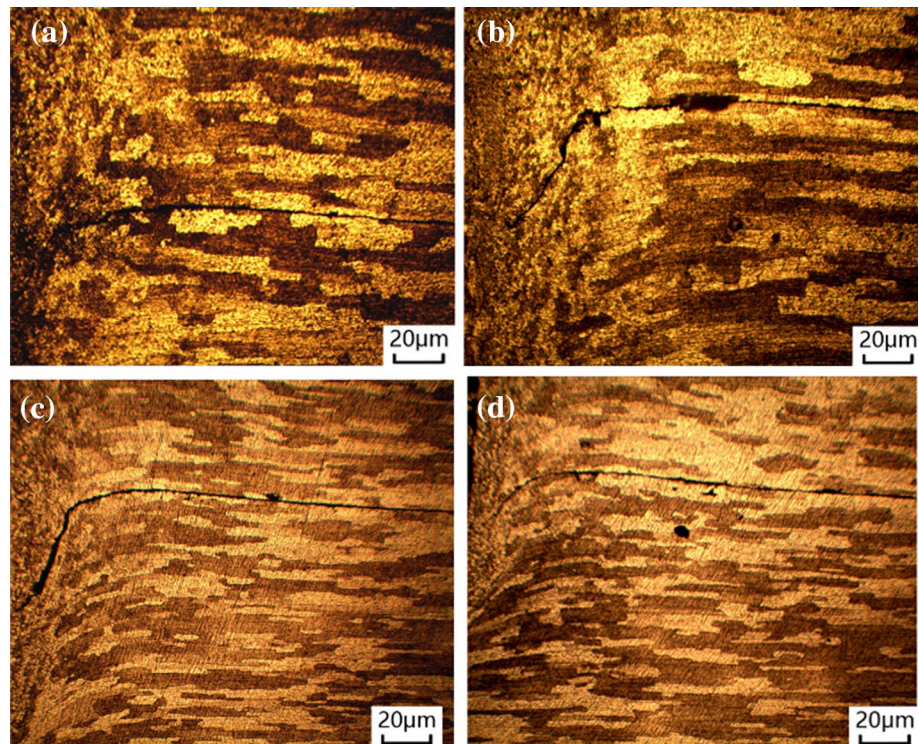


Fig. 6 Magnified images of the hook at different rotational speeds: **a** 2000, **b** 2200, **c** 2400 and **d** 2600 rpm

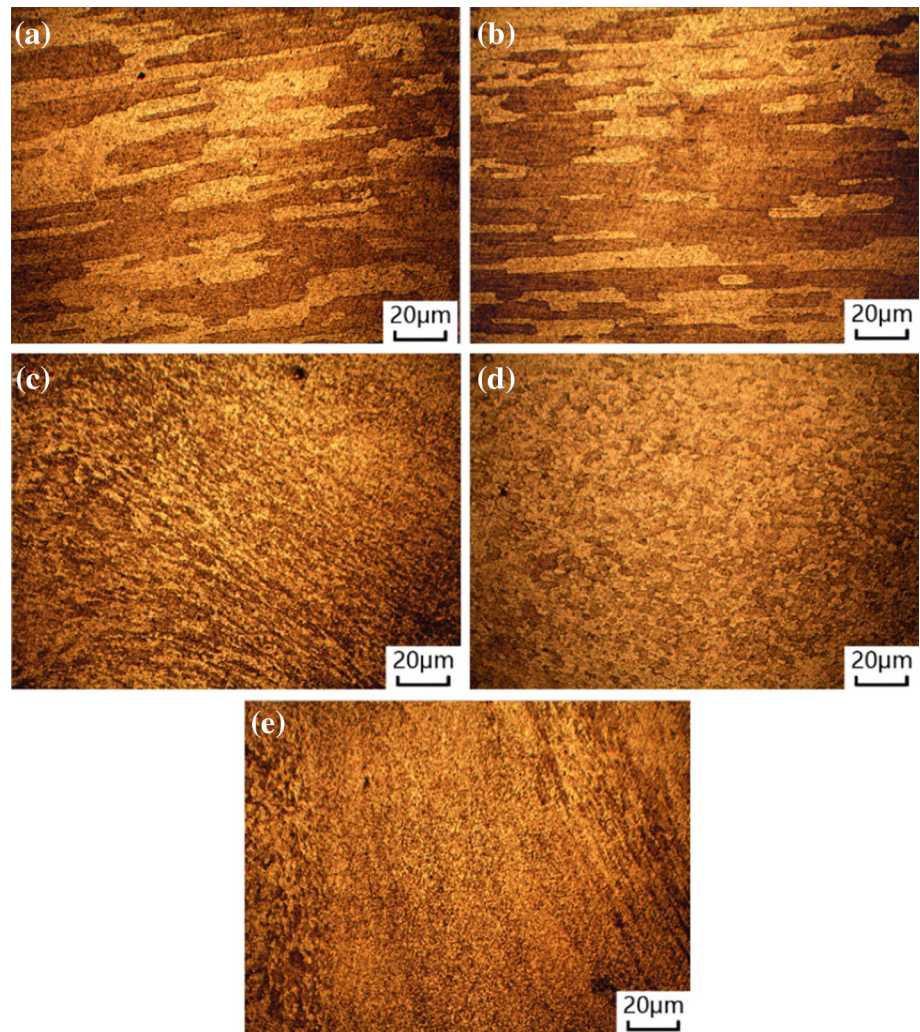


influence on the hook geometry. However, the bending level initially increased and then decreased with increasing rotational speed. This behavior could be attributed to different plastic deformations of the material at various heat inputs. The characteristics of the lap interface are further described in Sect. 3.3.

3.3 Analysis of Microstructures

As shown in the cross-section, the RFSSW joint can be divided into four regions, namely, BM, HAZ, TMAZ, and SZ. Figure 7 demonstrates the microstructures of these zones. Figure 7a shows that the grains in the BM are

Fig. 7 Microstructures of the joint at 2600 rpm: **a** BM, **b** HAZ, **c** TMAZ, **d** PAZ, and **e** SAZ



elongated along the rolling direction and exhibit irregular boundaries. Because HAZ experienced only the thermal cycle during the welding process, the zone had similar grain structures as that of the BM, but the grains were evidently coarsened. The grains in the TMAZ were driven by the sleeve and appeared distorted and elongated. Thus, incomplete dynamic recrystallization (DRX) developed because of the combined actions of a moderate thermal cycle and plastic deformation. Owing to close contact with the sleeve or pin, the materials in the SZ experienced numerous thermal cycles and severe plastic deformations. Consequently, complete DRX occurred in the SZ, and the SZ comprised equiaxed grains. Ji et al. [26] revealed that the materials near the inner and outer walls of the sleeve attained high flow velocity. However, the maximum velocity of the material appeared at the sleeve outer wall. The higher strain rate of the material led to smaller and finer grains in the SAZ (Fig. 7e) than those in the PAZ (Fig. 7d). As observed in various grain morphologies of Fig. 7, the microstructures on both sides of the SAZ/TMAZ interface were noticeable

different. The large difference in the microstructure of this interface led to structural stress as well as stress concentration during tensile tests.

In addition to the SAZ/TMAZ interface, the bottom of the SZ was also a weak region. Figure 8 shows the microstructures near the bottom of the SZ at various rotational speeds. Regions A and E marked in Fig. 8 are located at the bottom of the SAZ. Noticeable voids and bending material are observed in Region A. Similar to the TMAZ, the bending material was driven by the sleeve movement. In the Region E, the cracks extended to the SZ center, which was detrimental to the tensile properties of the joint. Regions B, C and D were close to the PAZ bottom, and the microstructures along the thickness were uneven. Similar to the microstructure distribution in both sides of the SAZ/TMAZ interface, we observed deformed grains in the TMAZ and coarsened grains in the HAZ below the SZ. Presumably, this region below the SZ at other rotational speeds has similar microstructure distribution because of the similarity in the welding process.

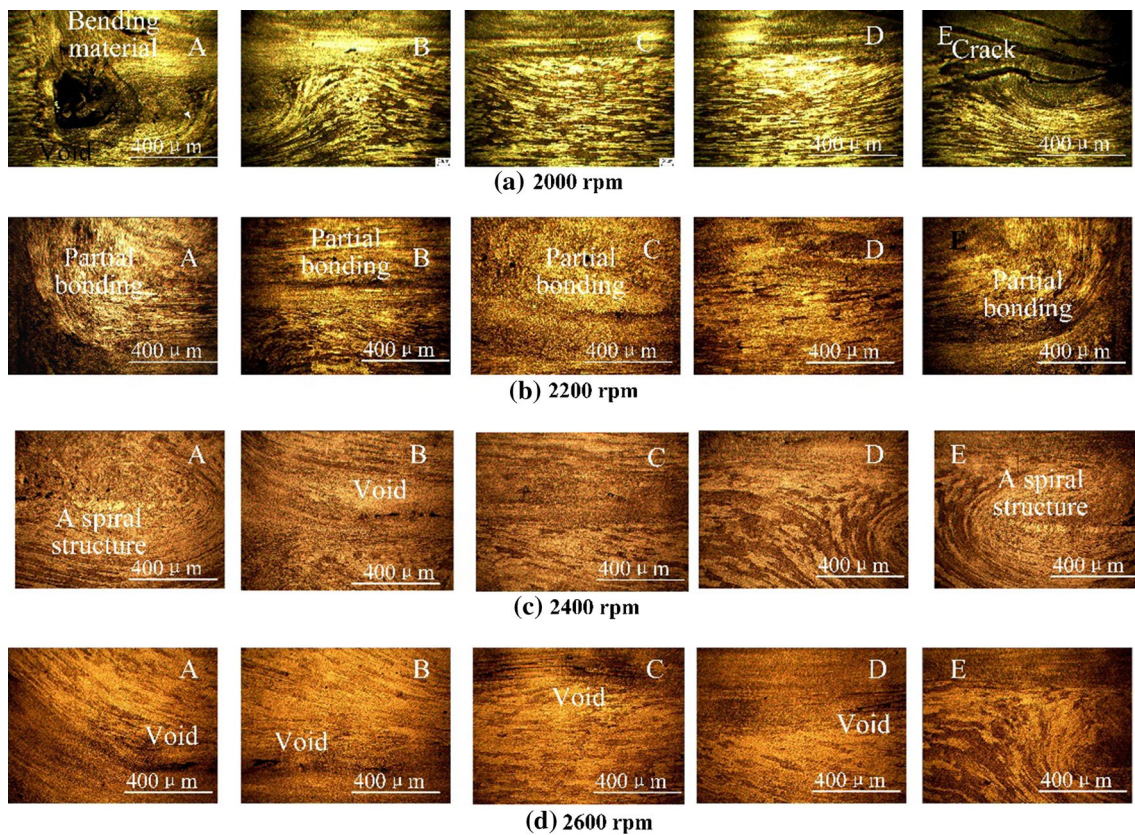


Fig. 8 Microstructures near the bottom of the SZ of joint at different rotational speeds: **a** 2000, **b** 2200, **c** 2400 and **d** 2600 rpm

Figure 8b–d show the microstructures of the joint at 2200–2600 rpm, the cracks and void in the Regions A and E evidently decreased. However, similar to the cracks, the movement trace of the sleeve and pin remained and then shrank to become slender and stripe. Specifically, it was a partial bonding, as shown in Fig. 8b. This partial bonding gradually became small from Region A to Region C, and then disappeared in region D, indicating the presence of a symmetrical cross-section. When the rotational speed increased to 2400 and 2600 rpm, the reduced partial bonding was shrunk to void in Regions B and C. Moreover, the material near the sleeve bottom showed a spiral structure (Fig. 8c, d).

3.4 Mechanical Properties of the RFSSW Joint

3.4.1 Microhardness Distributions

The peripheries of the SAZ and PAZ are weak regions, where a drastic change in the microstructures is observed. Figure 9 shows the microhardness measurement points in different regions. Figure 9a presents the measurement regions in the SAZ/TMAZ, SAZ, and SAZ/PAZ interfaces at 2200 rpm. Figure 10a shows the microhardness distributions

of these regions. As observed in figure, the hardness values of the SAZ were the highest possibly because of the presence of finer and smaller grains (Fig. 7e). Unlike the SAZ, the microhardness of the PAZ/SAZ interface slightly decreased. The lowest hardness values were located at the SAZ/TMAZ interface, which are possibly related to the elongated grains of the TMAZ. The microhardness values gradually decreased from the upper sheet to the lap interface at the previously mentioned regions, i.e., the regions near the defect with the minimum values.

Figure 9b, c show the microhardness measurement points of the cross-section of the other two rotational speeds. These points were located at the SAZ/TMAZ interface. The defective regions were discarded, as shown in Fig. 9b, c. Figure 10b shows the microhardness distribution of the SAZ/TMAZ interface at various rotational speeds. The microhardness values were partially reduced the lowest value at 2200 rpm, then increased to the highest value at 2400 rpm, and finally decreased at 2600 rpm. Furthermore, the microhardness gradually decreased along with the plate thickness. The minimum value was located at the tip of the void at 2200 rpm, and it was 109 HV only, whereas the microhardness at the tip of the void at 2400 rpm increased to the largest value of 157 HV. In contrast, the hardness values

Fig. 9 Microhardness measurement points at various rotational speeds: **a** 2200, **b** 2400, and **c** 2600 rpm

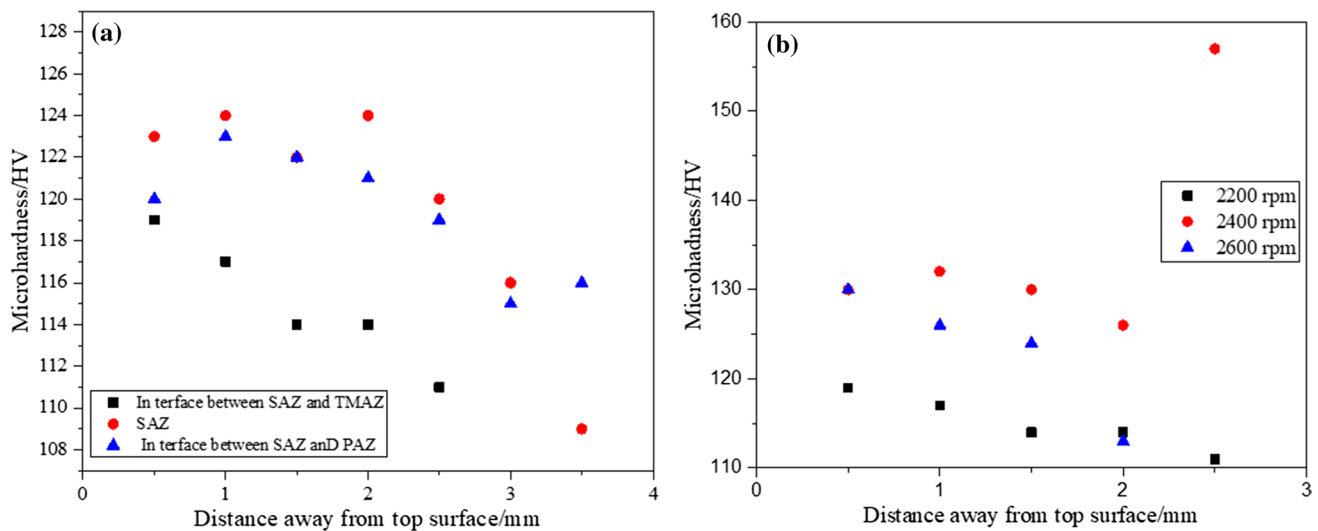
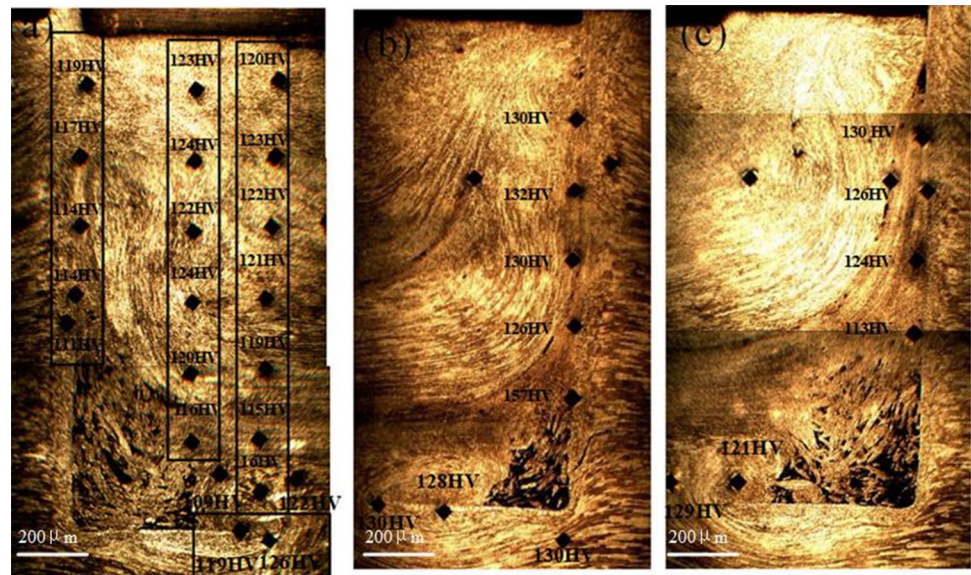


Fig. 10 Microhardness distributions of the RFSSW joints: **a** regions between PAZ and TMAZ as marked in Fig. 9a and **b** the SAZ/TMAZ interface at different rotational speeds

of the other regions away from the defect were only in the range of 120–130 HV. When the rotational speed increased to 2600 rpm, the hardness near the defect tip decreased to 113 HV. Therefore, the hardness values near the defect tip at the SAZ/TMAZ interface were 109, 157 and 113 HV at 2200, 2400 and 2600 rpm, respectively.

The microhardness near the defect tip of the lap interface was measured, as shown in Fig. 9. The microhardness distribution of lap interface at different rotational speeds has tendency similar to that at the SAZ/TMAZ interface. It initially increased from 2200 to 2400 rpm, and then decreased at 2600 rpm. A high rotational speed is advantageous for obtaining high heat input, thus facilitating the diffusion bonding of atoms at the interface. Excessive heat

can also weaken the material. However, the difference in hardness values was relatively small, i.e., 119, 128 and 121 HV at 2200, 2400 and 2600 rpm, respectively. Note that the microhardness values of the defect tip of the lap interface are higher than those at the SAZ/TMAZ interface at 2200 and 2600 rpm. However, an opposite result was obtained at 2400 rpm. The microhardness value of the defect tip at the SAZ/TMAZ interface was 157 HV, which is substantially higher than 128 HV at the bottom of the sleeve.

3.4.2 Tensile Properties of the RFSSW Joints

Figure 11 shows the lap shear strength (LSS) of the RFSSW joints at various rotational speeds. As observed in figure, the

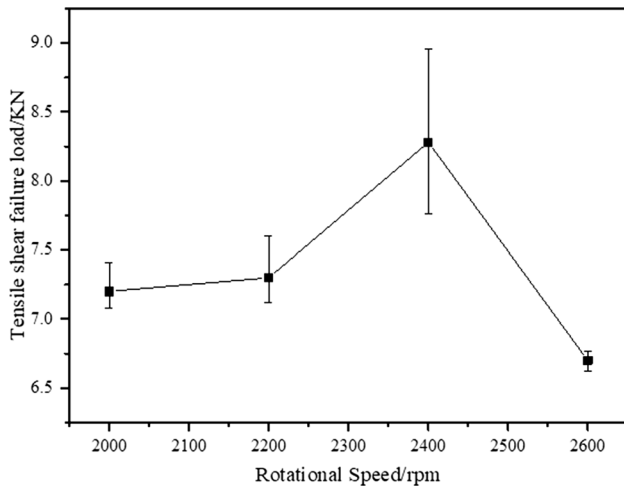


Fig. 11 Tensile-shear failure load of the RFSSW joints

mean LSS of the joint initially increases and then declined with increments in the rotational speed increased from 2000 to 2600 rpm. The maximum value was up to 8.80 kN at 2400 rpm, and the standard deviation of the mean LSS of the joint at 2400 rpm was 0.5028. When the rotational speed increased to 2600 rpm, the mean LSS value decreased to 6.77 kN, which is lower than that at 2000 rpm. The standard deviation of joint LSS at 2600 rpm (0.0572) was rather less than that at 2000 rpm (0.4614). The differences in the standard deviations of the LSS joints at various rotational speeds correspond to the error bars shown in Fig. 11. The large and small error bars coincide with the large and small standard deviations of the LSS joints at 2400 and 2600 rpm, respectively. Moreover, the standard deviations of the LSS joints are 0.4614 and 0.2135 at 2000 and 2200 rpm, respectively, which are larger than that at 2600 rpm and smaller than that at 2400 rpm. When compared with other aluminum–lithium alloys welded via the RFSSW, the largest LSS of 3.2-mm-thick joint is larger than 1.6-mm-thick 2198 aluminum–lithium alloys RFSSW joint [4], but smaller than 2-mm-thick 2198 aluminum–lithium alloys RFSSW joint because of the different materials used, thicknesses, and welding parameters [18, 27]. However, similar variation trends of the joint LSS at different rotational speeds were obtained [18].

Figure 12 shows the fracture surface morphologies of the tensile-shear specimens at different rotational speeds. Two types of fracture modes can be observed in this study. In the reported studies, all the RFSSW joints of the 2198 aluminum–lithium alloy at various rotational speeds exhibited the shear-plug fracture mode [18]. This plug fracture mode occurred when the plunge depth was changed [27]. Figure 12a, c illustrate that the tensile specimens at 2000 and 2400 rpm belong to the shear fracture mode. This is a common failure mode that shows the separation of upper and lower sheets. During the tensile-shear tests, all the joints

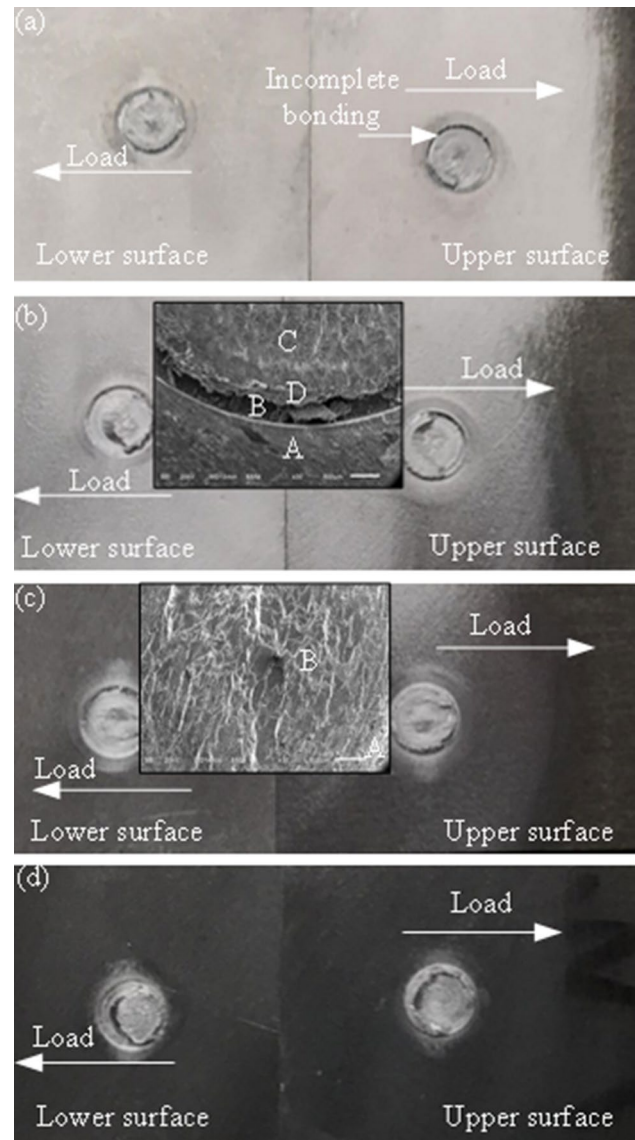


Fig. 12 Fracture surface morphologies of tensile specimens: **a** 2000, **b** 2200, **c** 2400 and **d** 2600 rpm

at 2000 and 2400 rpm generated the shear fracture. However, similar fracture modes in Fig. 12a, c corresponded to the minimum of 6.63 kN and maximum of 8.80 kN tensile-shear loads at 2000 and 2400 rpm, respectively. Furthermore, some differences existed in the fracture path. At low rotational speed (2000 rpm), the SZ material and hook were separated by void, as shown in Fig. 4a. The cracks marked in Fig. 4a propagated into the SZ and then connected to the void at the bottom of the SAZ. Therefore, the tensile-shear specimen at 2000 rpm fractured at the lap interface, which is primarily dependent on the welding defects. In the fractured surface, we observed an incomplete bonding at the bottom surface of the upper sheet, as shown in Fig. 12a. For the tensile specimen at 2400 rpm, hook tip and void at the

SAZ bottom were two potential initiation sites. The nucleation sites always propagated toward the direction with the minimum resistance based on the law of minimum resistance. Regarding the microstructure distribution difference, the spiral structure at the bottom of the SZ indicates the existence of obvious partial bonding (Fig. 8c), whereas the SAZ/TMAZ interface was bonded appropriately (Fig. 5c). Furthermore, the microhardness of the defect tip in the SAZ/TMAZ interface was higher than that at the bottom of the SAZ (Fig. 9). These two reasons led the cracks to extend to the bottom of the SZ. The large microstructure difference at the SZ bottom also generated uneven deformation and then resulted in shear stress perpendicular to the loading direction. Consequently, the crack propagated along the bottom of the SZ, and the upper and lower sheets were split. The fracture mechanisms vary even if similar fracture modes of tensile shear specimens were observed at 2000 and 2400 rpm. Figure 15a shows the fracture location of the joint at 2400 rpm. Note that the SAZ/TMAZ interface existed crack-free region in the fracture location of joint, demonstrating that higher tensile-shear load of joint at 2400 rpm.

The tensile-shear specimens at 2200 and 2600 rpm, they had a similar fracture path, and all the joints exhibited tensile-shear mixed fracture. The tensile-shear loads of the lap joint at 2200 and 2600 rpm were 7.12 and 6.62 kN, respectively. According to the nomenclature adopted in the literature, this fracture mode occurred as through the weld but was not completely similar to that reported by Campanella et al. [23]. In this study, the crack at the bottom of the SAZ

developed parallel to the loading direction and propagated toward a surface, thus generating a typical shear zone at 45° from the loading direction. Subsequently, the crack turned to the lap interface parallel to the loading direction to form a “Z” shape fractured surface owing to the partial removal of the SZ on the lower sheet. Figure 15b shows the fracture location of joint at 2600 rpm. Evidently, crack initiation, propagation and fracture were along the lap interface and the bottom of the SAZ. Furthermore, the crack in the sleeve retreating path decreased load capacity of joint.

The incomplete bonding area in Fig. 12b, d is smaller than that in Fig. 12a. As shown in the magnified image of Fig. 12b, the region near the defect can be divided into four parts, i.e., Region A–Region D. Figure 13 shows the SEM images of the four regions in Fig. 12b. Regions A, B, and D are near the defect, and their surfaces are flat. Evidently, the material is not bonded; hence, the crack may initiate and propagate along this area. Region C located at the PAZ develops an elongated parabolic shape owing to the microstructure and applied loading mode. Note that this region had been joined with the adjacent material. Figure 14 shows the fracture surface morphology of the tensile-shear specimen at 2400 rpm. Various fracture surfaces presented dimples, indicating the ductile fracture of the tensile-shear specimen.

Figure 15 shows the fracture locations of the RFSSW joints at 2400 and 2600 rpm. As mentioned previously, the hook and welding defects depend on the crack initiation of the tensile-shear specimens. At the fractured cross section, the material near the downward hook and welding defects

Fig. 13 Fracture surface morphology of the tensile-shear specimen at 2200 rpm: **a–d** correspond to Regions A–D as marked in Fig. 12b

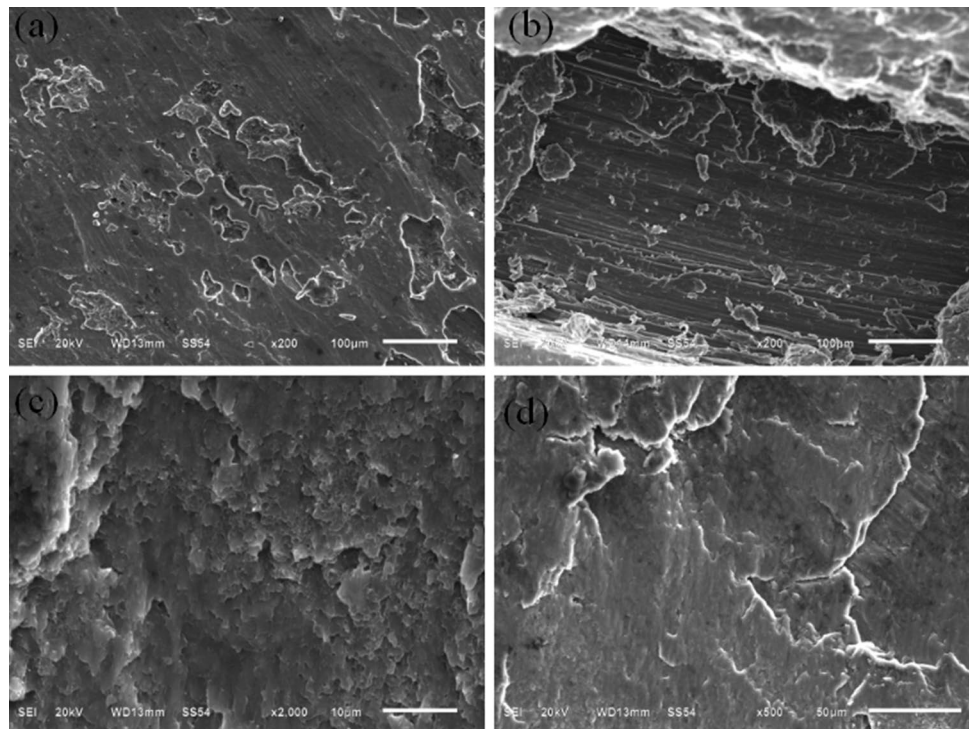


Fig. 14 Fracture surface morphology of the tensile-shear specimen at 2400 rpm: **a, b** correspond to Regions A–B as marked in Fig. 12c

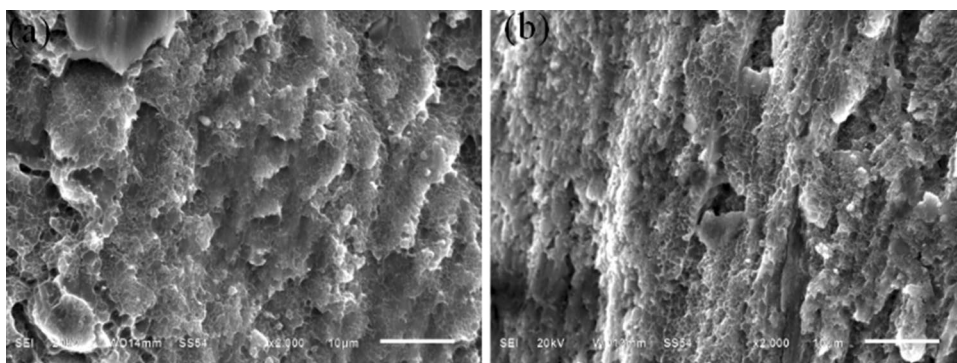
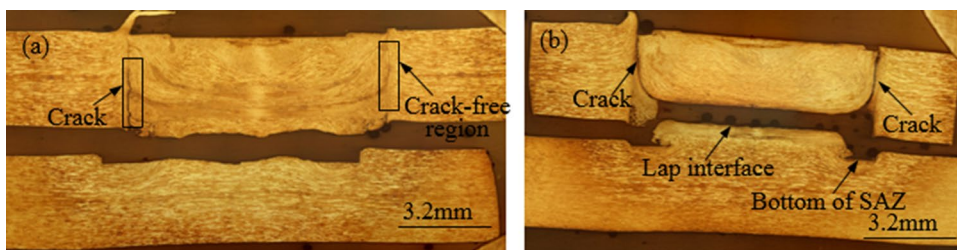


Fig. 15 Fracture locations of the RFSSW joints at: **a** at 2400 and **b** 2600 rpm



was discontinuous, and the crack easily initiated from the hook with extra load because of the sharp tip. The initiated crack propagated along the bottom of the SAZ where the incomplete bonding was located. Therefore, partial fractured areas existed at the bottom of the SAZ (Fig. 15). The crack was in contact with the bending material at the bottom of the SAZ and SAZ/PAZ interfaces, which can explain the wedged fracture surface. With crack propagation, the incomplete bonding at the lap interface (Fig. 8b) developed a convenient path to make the crack grow, and then the tensile-shear specimen fractured. When the rotational speed increased to 2400 rpm, the defect in the lap interface reduced, and a large heat input facilitated a diffusion bonding, leading to the strengthened lap interface corresponding to the ductile fracture of the tensile-shear specimen in Fig. 14. However, a large volume of heat input at 2600 rpm also resulted in the weakening of the material (Fig. 10). Furthermore, the large void at the bottom of the SAZ led to the same fracture mode as that at 2200 rpm.

4 Conclusions

RFSSW was used to join 3.2-mm-thick 2060 aluminum alloys. The macrostructure, microstructures and mechanical properties of the RFSSW joint were investigated in this study. The following conclusions can be drawn.

1. 2060 Aluminum alloys sheets were successfully welded using RFSSW. The annular groove around the periphery of the sleeve is observed at 2000 rpm, and then dis-

appears with increasing rotational speed. The hook is downward bending. The void at the bottom of the SAZ initially increases and then decreases with the increments in the rotational speed.

2. The RFSSW joint can be divided into SAZ, PAZ, TMAZ, HAZ and BM. The microstructure distribution at the bottom of the SZ is similar to that in the SAZ/TMAZ interface, containing fine, elongated distorted, and coarsened grains. This uneven distribution is responsible for the stress concentration and nonuniform deformation.
3. The microhardness values gradually decrease along with the thickness, and the microhardness also declines at the SAZ, SAZ/PAZ and SAZ/TMAZ interfaces. Furthermore, the microhardness values of the SAZ/TMAZ interface initially increase and then decrease with increments in rotational speed from 2200 to 2600 rpm.
4. The tensile-shear failure load initially increases and then decreases with increments in rotational speed from 2200 to 2600 rpm. The maximum load is up to 8.8 kN at 2400 rpm. Moreover, similar fracture mode does not indicate the same tensile-shear load. The fracture path is related to the microstructure distribution, microhardness, material flow, and welding defects.

Acknowledgements This work was supported by the AVIC Manufacturing Technology Institute under Grant MJ-2016-G-63.

References

1. Z.Z. Chen, M. Li, X.G. Ma, Y. Xiao, *Adv. Mater. Res.* **842**, 466 (2014)
2. D. He, K. Yang, M. Li, H. Guo, N. Li, R. Lai, S. Ye, *Sci. Technol. Weld. Join.* **18**, 610 (2013)
3. Z.H. Guo, G.Y. Zhao, L.M. Ke, L.Z. Xing, *Adv. Mater. Res.* **346**, 314 (2011)
4. C.C. de Castro, A.H. Plaine, N.G. de Alcântara, J.F. dos Santos, *Int. J. Adv. Manuf. Technol.* **99**, 1927 (2018)
5. Y. Lin, Z.Q. Zheng, S.C. Li, X. Kong, Y. Han, *Mater. Charact.* **84**, 88 (2013)
6. R.J. Rioja, J. Liu, *Metall. Mater. Trans. A* **43**, 3325 (2012)
7. A.J. Beaudoin, M. Obstalecki, W. Tayon, M. Hernquist, R. Mudrock, P. Kenesei, U. Lienert, *Acta Mater.* **61**, 3456 (2013)
8. G. Pieta, J. dos Santos, T.R. Strohaecker, T. Clarke, *Mater. Manuf. Process.* **29**, 934 (2014)
9. D. Kim, H. Badarinarayan, I. Ryu, J.H. Kim, C. Kim, K. Okamoto, R.H. Wagoner, K. Chung, *Met. Mater. Int.* **16**, 323 (2010)
10. P.B. Prangnell, D. Bakavos, *Mater. Sci. Forum* **638**, 1237 (2010)
11. Y.F. Sun, H. Fujii, N. Takaki, Y. Okitsu, *Sci. Technol. Weld. Join.* **16**, 605 (2013)
12. B. Han, Y. Huang, S. Lv, L. Wan, J. Feng, G. Fu, *Mater. Des.* **51**, 25 (2013)
13. S. Ji, X. Meng, Y. Zeng, L. Ma, S. Gao, *Mater. Des.* **97**, 175 (2016)
14. Y.Q. Zhao, H.J. Liu, Z. Lin, S.X. Chen, J.C. Hou, *Sci. Technol. Weld. Join.* **19**, 617 (2014)
15. A.H. Plaine, U. Suhuddin, N.G. de Alcântara, J.F. dos Santos, *Int. J. Adv. Manuf. Technol.* **92**, 2 (2017)
16. Z.K. Shen, X.Q. Yang, S. Yang, Z.H. Zhang, Y.H. Yin, *Mater. Des.* **54**, 766 (2014)
17. L. Zhou, L.Y. Luo, T.P. Zhang, W.X. He, Y.X. Huang, J.C. Feng, *Int. J. Adv. Manuf. Technol.* **92**, 3452 (2017)
18. Y. Shi, Y.M. Yue, L.G. Zhang, S.D. Ji, Y. Wang, *Trans. Indian Inst. Metals* **71**, 139 (2018)
19. B. Cai, Z.Q. Zheng, D.Q. He, S.C. Li, H.P. Li, *J. Alloy. Compd.* **645**, 15 (2015)
20. J.W. Peng, W.D. Li, M. Wan, C.S. Zhang, J. Li, G.G. Su, *Int. J. Mater. Form.* **269**, 20 (2017)
21. Z.K. Shen, X.Q. Yang, Z.H. Zhang, L. Cui, T.L. Li, *Mater. Des.* **44**, 476 (2012)
22. T. Rosendo, B. Parra, M.A.D. Tier, A.A.M. da Silva, J.F. dos Santos, T.R. Strohaecker, N.G. Alcântara, *Mater. Des.* **32**, 1094 (2011)
23. L.C. Campanelli, U.F.H. Suhuddin, A.I.S. Antonialli, J.F. dos Santos, N.G. de Alcântara, C. Bolfarini, *J. Mater. Process. Technol.* **213**, 515 (2013)
24. B. Parra, V.T. Saccon, N.G.D. Alcântara, *Tecnol. Metal. Mater. Min.* **8**, 184 (2011)
25. Z. Li, S. Ji, Y.N. Ma, P. Chai, Y.M. Yue, S.S. Gao, *Int. J. Adv. Manuf. Technol.* **86**, 1925 (2016)
26. S.D. Ji, Y. Wang, Z.W. Li, Y.M. Yue, P. Chai, *Trans. India Inst. Metals* **70**, 1417 (2017)
27. Y.M. Yue, Y. Shi, S.D. Ji, Y. Wang, Z.W. Li, *J. Mater. Eng. Perform.* **5064**, 26 (2017)

Publisher's Note Springer Nature remains neutral with regard to jurisdictional claims in published maps and institutional affiliations.